To appear in Journal of the Mechanics and Physics of Solids (DOI: 10.1016/j.jmps.2025.106232)

Impact of Gas/Liquid Phase Change of CO_2 during Injection for Sequestration

Mina Karimi,[1,*] Elizabeth Cochran,[2] Mehrdad Massoudi,[3] Noel Walkington,[4] Matteo Pozzi,[5] and Kaushik Dayal[5,4,6]

[1]*Department of Mechanical Engineering, Purdue University*
[2]*U. S. Geological Survey, Earthquake Science Center*
[3]*National Energy Technology Laboratory*
[4]*Center for Nonlinear Analysis, Department of Mathematical Sciences, Carnegie Mellon University*
[5]*Department of Civil and Environmental Engineering, Carnegie Mellon University*
[6]*Department of Mechanical Engineering, Carnegie Mellon University*

(Dated: June 19, 2025)

CO_2 sequestration in deep saline formations is an effective and important process to control the rapid rise in CO_2 emissions. The process of injecting CO_2 requires reliable predictions of the stress in the formation and the fluid pressure distributions – particularly since monitoring of the CO_2 migration is difficult – to mitigate leakage, prevent induced seismicity, and analyze wellbore stability. A key aspect of CO_2 is the gas-liquid phase transition at the temperatures and pressures of relevance to leakage and sequestration, which has been recognized as being critical for accurate predictions but has been challenging to model without *ad hoc* empiricisms.

This paper presents a robust multiphase thermodynamics-based poromechanics model to capture the complex phase transition behavior of CO_2 and predict the stress and pressure distribution under super- and sub- critical conditions during the injection process. A finite element implementation of the model is applied to analyze the behavior of a multiphase porous system with CO_2 as it displaces the fluid brine phase. We find that if CO_2 undergoes a phase transition in the geologic reservoir, the spatial variation of the density is significantly affected, and the migration mobility of CO_2 decreases in the reservoir. A key feature of our approach is that we do not *a priori* assume the location of the CO_2 gas/liquid interface – or even if it occurs at all – but rather, this is a prediction of the model, along with the spatial variation of the phase of CO_2 and the change of the saturation profile due to the phase change.

1. Introduction

Carbon dioxide (CO_2) sequestration and storage in geological formations is among the most promising available approaches to reduce CO_2 emissions [1]. The CO_2 emitted from different industrial sources can be collected and isolated in deep underground formations [2], or injected into depleted natural gas reservoirs to enhance gas recovery [3]. Of the various types of geological formations that are considered for CO_2 storage, saline aquifers appear to provide the most storage capacity for CO_2 [4]. However, there remain several fundamental challenges [1].

CO_2 is typically injected into deep, brine-saturated formations in a dense, supercritical state, as the lower viscosity of supercritical CO_2 compared to its liquid phase makes it easier to inject. The higher density of the resident brine drives the injected CO_2 to migrate upward toward the top of the reservoir, where it is ideally trapped beneath the caprock. The migration of CO_2 and brine involves more complex processes over longer timescales. CO_2 can gradually dissolve into the resident brine, forming a denser and more reactive fluid that sinks through convective mixing, reducing the risk of leakage. The CO_2-brine interaction is coupled with a series of geochemical reactions with the surrounding subsurface material, leading to alteration in transport properties such as porosity and permeability through dissolution and precipitation processes [5–10].

Prior Work. Reliable predictions, based on numerical simulations, are needed to predict CO_2 propagation in deep underground formations and estimate the capacity of storage to reduce possible leakage risks [11]. Further, injecting supercritical CO_2 into deep geological formations can increase fluid pressure near injection wells, alter the stress regime along pre-existing faults, potentially leading to fault activation and induced seismicity [11, 12]. Such seismic events can compromise the integrity of the underground reservoir and caprock, posing a risk of CO_2 leakage to shallower layers [13, 14]. Consequently, accurately predicting the spatial distribution of pressure, CO_2 phase, and density is essential for ensuring the safety of CO_2 storage.

Several studies have proposed numerical models to investigate the subsurface transport of injected CO_2, focusing primarily on fluid transport while often neglecting the effect of deformation of the porous medium [15–19]. These models usually simplify fluid saturation-pressure relationships and CO_2 properties, commonly assuming CO_2 to remain in a supercritical state at constant temperatures [20–23]. While other studies account for coupled fluid transport and matrix deformation, they still depend on simplified constitutive models for pressure-saturation relations and fluid properties [16, 18, 24–29]

In general, simulation of phase transformation in fluids is challenging because of the significant change in the density and viscosity values, the evolving interfaces between liquid and gas, and the complex behavior of the liquid/gas mixture. Recently,

---

[*] minakari@alumni.cmu.edu

free energy-based approaches have been proposed to predict the phase transformation of fluids for different applications. For instance, Ateshian and Shim developed an energy-based formulation with particular emphasis on the jump conditions across the interface of liquid and gas phases [30]; Hu et al. proposed a formulation based on the Navier-Stokes-Korteweg equations to simulate the liquid-vapor phase transition under non-equilibrium conditions [31]; and we presented a variational energy-based model for multi-phase flow which models the behavior of phase-changing fluids in a porous medium [32].

Most prior studies of CO_2 sequestration ignore the CO_2 phase transition to simplify the flow analysis; however, it can cause considerable error, specifically for short-term, high-rate injections and in shallower reservoirs. Some studies consider the phase transition of CO_2 during injection and can be broadly categorized into three approaches. The first approach assumes a constant density for the liquid phase of CO_2 and typically combines the empirical Brooks-Corey model, that provides a relationship between fluid pressure and phase saturation, with the equation of state for CO_2 e.g., [33, 34]; this assumption can introduce considerable errors in predicting pressure and density profiles. The second approach employs a multi-phase flow by considering phase partitioning criteria to simulate the CO_2 phase change. This approach considers a pressure threshold to define different phases (e.g., TOUGH simulators [35–37]); however, the use of a sharp threshold in the subcritical regions, where CO_2 pressure is close to the critical pressure, can lead to unstable behavior, abrupt changes in properties, and CO_2 phase change with small perturbations. The third approach focuses on studying the phase change of CO_2 during injection by using multi-phase flow models to simulate the behavior of CO_2 in both its liquid and gas states and accounting for the phase transition of CO_2 by considering the variation in the enthalpy of the CO_2 liquid and gas phases, which requires the calculation of internal energy for each phase, e.g. [38–40]; however, these models are typically limited to simulating the behavior of CO_2 in the injector.

Contributions of This Paper. Typically, CO_2 is stored in the supercritical phase in deep saline formations at depths of $800\,\mathrm{m}$ to $3\,\mathrm{km}$. However, in a large reservoir, CO_2 can migrate to shallower depths [41], and also leakage of CO_2 from the reservoir to faults or abandoned wellbores and upward migration of CO_2 to the ground surface can decrease the temperature and pressure and lead to subcritical conditions [35, 36, 42]. Sub-critical conditions of CO_2 at depths shallower than $500 - 750\ \mathrm{m}$ can provide a mixture of CO_2 phases (gas, liquid, and super-critical), creating a complicated multi-phase flow process.

In this work, we investigate the complex behavior of multiphase CO_2 flow that consistently accounts for the CO_2 phase transition using an approach based on the thermodynamical free energy [32]. Our approach enables accounting of the entire mixture of CO_2 phases without any *ad hoc* assumptions on the behavior of CO_2 and using a minimal set of state variables. We use the simple yet effective van der Waals (vdW) model to simulate the complex behavior and phase transition of CO_2 under sub-critical conditions. The free-energy-based formulation and the vdW model allow us to simulate the transition from the gas to the liquid phase of CO_2 at different temperatures. This approach consistently provides fluid pressure-density relations without relying on additional *ad hoc* assumptions, therefore preventing unstable behavior and oscillations during the phase transition. We study the impact of the CO_2 phase transition on the pressure, saturation, density distributions, and migration mobility of CO_2 in a geological formation. We also investigate the upward mobility of gas-liquid CO_2 and supercritical CO_2 in the event of leakage. In Appendix B, we briefly compare the approach proposed in this paper with conventional multiphase methods.

2. Model Formulation

We consider CO2 injected into a saturated saline reservoir containing incompressible brine with a deformable solid skeleton. To simulate this multiphase fluid unsaturated system, we use the energetic formulation developed by Karimi et al. [32]. We assume that our system consists of three distinct immiscible components: the solid skeleton, CO_2, and the brine fluid phases, indexed by subscripts s, c, and b, respectively. For simplicity, we neglect chemical reactions and assume isothermal conditions.

The overall structure of our approach is variational; while different from the usual Coleman-Noll procedure, it provides an approach that is equally consistent with thermodynamics [43]. We begin with a free energy that is formulated in Section 2.B and has contributions from the solid skeleton as well as the fluid phases. From this energy, the mechanical response, corresponding to momentum balance, is obtained by setting to zero the variation of the energy with respect to the deformation. The fluid response is obtained by defining the chemical potential as the variation of the energy with respect to the fluid density, and then relating to fluid velocity to the gradient of the chemical potential. Finally, the variation of the energy with respect to the volume fraction provides the local balance of fluid pressure, i.e., at a given spatial location, the pressure must be equal in all of the fluid phases. Finally, we discuss briefly in Section 2.G the non-negativity of the dissipation.

2.A. Kinematics and Notation

We use the subscript $\cdot_0$ to refer to quantities and differential operators in the reference configuration. We define the deformation through the referential position $\boldsymbol{x}_0$, the deformed position $\boldsymbol{x}(\boldsymbol{x}_0, t)$, and the displacement $\boldsymbol{u}(\boldsymbol{x}_0, t) := \boldsymbol{x}(\boldsymbol{x}_0, t) - \boldsymbol{x}_0$. Then, we have the deformation gradient tensor $\boldsymbol{F} = \dfrac{\partial \boldsymbol{x}}{\partial \boldsymbol{x}_0}$ and the Jacobian $J = \det \boldsymbol{F}$.

We define two densities for each fluid phase i: the mass of the fluid phase per unit deformed volume of the entire mixture, denoted $\mathcal{R}_i$; and the mass of the fluid phase per unit deformed volume occupied by that phase, denoted the "true" density ρ_i. These are related by $\mathcal{R}_i = \phi_i \rho_i$, where ϕ_i is the volume fraction of phase i. The relations between referential and current quantities, following the assumption of affine transformation [32, 44–46], are $\mathcal{R}_i = J^{-1}\mathcal{R}_{0i}$ and $\rho_i = \dfrac{\phi_{0i}}{\phi_i} J^{-1}\rho_{0i}$.

2.B. Energetics

The thermodynamic free energy of the system is defined as:

$$\mathcal{E}\left[\boldsymbol{x}, \mathcal{R}_{0c}, \phi_c\right] = \int_{\Omega_0} \Big(W_{0s}\left(\boldsymbol{F}\right) + W_{0c}\left(\mathcal{R}_{0c}, \phi_c, J\right) + \frac{\epsilon}{2}|\nabla_0 \mathcal{R}_{0c}|^2 - \boldsymbol{b}_0 \cdot \boldsymbol{x} \Big) \, \mathrm{d}\Omega_0 \tag{2.1}$$

where W_{0s} and W_{0c} are the (Helmholtz) free energies per unit referential volume of the skeleton and the CO_2, respectively; the brine is assumed to be incompressible, and therefore, its free energy does not appear. The potential due to gravity is given by $\boldsymbol{b}_0 \cdot \boldsymbol{x}$, where $\boldsymbol{b}_0 = \mathcal{R}_0 \boldsymbol{g} = \left(\mathcal{R}_{0s} + \mathcal{R}_{0c} + \mathcal{R}_{0b}\right)\boldsymbol{g}$ is the body force due to gravity $\boldsymbol{g}$. The gradient term with the coefficient ϵ is a phase-field-like regularization to account for the surface energy of the CO_2 gas/liquid interface and provide smoothing to allow the use of straightforward computational methods that do not need to track free boundaries [47]. This energy includes contributions due to the deformation of the solid skeleton as well as due to changes in volume of the (compressible) fluid phases.

The solid skeleton is modeled using a simple compressible neo-Hookean free energy:

$$W_{0s}(\boldsymbol{F}) = \phi_s \left(\frac{\mu}{2}(\mathrm{tr}(\boldsymbol{F}^T\boldsymbol{F}) - 2) - \mu \log J + \frac{\lambda}{2}(\log J)^2 \right) \tag{2.2}$$

where μ and λ are the Lame elastic constants. The CO_2 is modeled using the vdW free energy in the setting of hyperelasticity by the expression [32, 48]:

$$W_{0c}(\mathcal{R}_{0c}, \phi_c, J) = c\mathcal{R}_{0c}\bar{R}T\left(1 - \log(c\bar{R}T)\right) - \mathcal{R}_{0c}\bar{R}T \log\left(\frac{J\phi_c}{\mathcal{R}_{0c}} - b \right) - a\frac{\mathcal{R}_{0c}^2}{J\phi_c} \tag{2.3}$$

where $\bar{R}$ is the ideal gas constant; T is the temperature; c is a non-dimensional constant, and a and b are constants that relate to the phase transition.

While we have made specific constitutive choices above, the proposed framework is general and allows for the use of different free energy models. In Appendix A, we compare the simple vdW model against the for an explanation of simulating CO_2 phase using the Peng-Robinson free energy model.

2.C. Incompressibility of Brine

The incompressibility of brine introduces a geometric constraint. The volume fractions of CO_2, skeleton, and brine must satisfy $\phi_s + \phi_c + \phi_b = 1$. Since the solid phase deforms affinely, we have that $\phi_s = \phi_{0s}$, i.e., the volume fraction in the deformed configuration is equal to the volume fraction in the reference configuration. For the incompressible brine, we require that the true density in the current configuration have a fixed value ρ_b, giving $\phi_b = \dfrac{\mathcal{R}_{0b}}{J\rho_b}$. Together, these provide the relation $\phi_c + \phi_{0s} + \dfrac{\mathcal{R}_{0b}}{J\rho_b} = 1$. We enforce the constraint by using a Lagrange multiplier p that corresponds to the fluid pressure in the brine. We define the Lagrangian functional as follows:

$$\mathcal{L}[\boldsymbol{x}, \mathcal{R}_{0c}, \mathcal{R}_{0b}, \tilde{\phi}_c, p] = \int_{\Omega_0} \left(W_{0s}\left(\boldsymbol{F}\right) + W_{0c}\left(\mathcal{R}_{0c}, \tilde{\phi}_c\right) + \frac{\epsilon}{2}|\nabla_0 \mathcal{R}_{0c}|^2 - \boldsymbol{b}_0 \cdot \boldsymbol{x} + p\left(\tilde{\phi}_c + J\phi_{0s} + \frac{\mathcal{R}_{0b}}{\rho_b} - J \right) \right) \mathrm{d}\Omega_0 \tag{2.4}$$

For mathematical simplicity, we define $\tilde{\phi}_c = J\phi_c$ as a primary variable.

2.D. Fluid Transport

We obtain the chemical potentials of the CO_2 and brine by taking the variational/functional derivative of the Lagrangian (2.4) with respect to $\mathcal{R}_{0i}$ [32, 44, 49]:

$$\eta_{0c} = -\frac{\partial W_{0c}}{\partial \mathcal{R}_{0c}} + \boldsymbol{g} \cdot \boldsymbol{x} - \epsilon \, \mathrm{div}_0(\nabla_0 \mathcal{R}_{0c}) \qquad \text{and} \qquad \eta_{0b} = -\frac{p}{\rho_b} + \boldsymbol{g} \cdot \boldsymbol{x} \tag{2.5}$$

The referential relative velocity vector for each fluid phase is defined as $\boldsymbol{v}_{0i} = \boldsymbol{K}_i \nabla_0 \eta_{0i}$, where $\boldsymbol{K}_i$ is the referential permeability. The permeability in the current configuration is $\boldsymbol{k}_i = J^{-1}\boldsymbol{F}\boldsymbol{K}_i\boldsymbol{F}^\top$, and $\boldsymbol{k}_i = \dfrac{\kappa}{\gamma_i}\rho_i \boldsymbol{I}$ with κ the true permeability; γ_i the dynamic viscosity of the fluid; and $\boldsymbol{I}$ is the second-order identity tensor. The viscosity of each fluid phase is assumed to be constant. Consequently, using the relation $\boldsymbol{q}_{0i} = \mathcal{R}_i \boldsymbol{v}_{0i}$ for the referential fluid flux vector, we have the flux vectors for the CO$_2$ and brine:

$$\boldsymbol{q}_{0c} = -\boldsymbol{K}_c \left(\mathcal{R}_c \nabla_0 \frac{\partial W_{0c}}{\partial \mathcal{R}_{0c}} - \mathcal{R}_c \boldsymbol{F}^\top \boldsymbol{g} + \epsilon \mathcal{R}_c \nabla_0 \operatorname{div}_0 (\nabla_0 \mathcal{R}_{0c}) \right) \qquad \text{and} \qquad \boldsymbol{q}_{0b} = -\boldsymbol{K}_b \left(\phi_b \nabla_0 p - \mathcal{R}_b \boldsymbol{F}^\top \boldsymbol{g} \right) \tag{2.6}$$

Finally, using the conservation of mass for each fluid phase, we can write the governing PDE:

$$-\int_{\partial \Omega} \boldsymbol{q}_i \cdot \boldsymbol{n} \, \mathrm{d}S = \frac{\mathrm{d}}{\mathrm{d}t} \left(\int_{\Omega} \mathcal{R}_i \, \mathrm{d}V \right) \implies -\operatorname{div}_0 \boldsymbol{q}_{0i} = \frac{\mathrm{d}}{\mathrm{d}t} \mathcal{R}_{0i} \tag{2.7}$$

which is the generalization of the standard Darcy law, which is the simplest model for fluid transport in rigid porous media.

We highlight that the surface energy contribution leads to a third-order derivative in the CO$_2$ flux vector in $(2.6)_1$ and, consequently, a fourth-order derivative in the balance of mass for the CO$_2$ phase (2.7). To be able to use a standard finite element approach, we use a mixed method by introducing $\psi := \operatorname{div}_0 (\nabla_0 \mathcal{R}_{0c})$, as discussed further in Section 2.H.

2.E. Balance of Linear Momentum

Setting to zero the variational derivative of the Lagrangian functional (2.4) with respect to $\boldsymbol{x}$ gives the balance of momentum:

$$\operatorname{div}_0 \boldsymbol{T} + \boldsymbol{b}_0 = \boldsymbol{0} \tag{2.8}$$

where we have defined $\boldsymbol{T} := \dfrac{\partial W_{0s}}{\partial \boldsymbol{F}} + \dfrac{\partial W_{0c}}{\partial \boldsymbol{F}}$, the first Piola stress tensor. This corresponds to the total stress and consists of contributions from the elasticity of the solid skeleton and from the volume changes of the compressible fluids. For the constitutive choices in (2.2) and (2.3), we have the expression:

$$\boldsymbol{T} = \phi_{0s} \left(\mu \boldsymbol{F} - \mu \boldsymbol{F}^{-\top} + \lambda \log J \boldsymbol{F}^{-\top} \right) - (1 - \phi_{0s}) p J \boldsymbol{F}^{-\top} \tag{2.9}$$

The balance of angular momentum is automatically satisfied by the choice of a frame indifferent energy density in (2.1). That is, since the energy densities in (2.2) and (2.3) are invariant under the transformation $\boldsymbol{F} \to \boldsymbol{QF}$, for every rotation $\boldsymbol{Q}$, it follows that the stress $\boldsymbol{T} := \dfrac{\partial W_{0s}}{\partial \boldsymbol{F}} + \dfrac{\partial W_{0c}}{\partial \boldsymbol{F}}$ satisfies the symmetry requirement $\boldsymbol{T}\boldsymbol{F}^\top = \boldsymbol{F}\boldsymbol{T}^\top$.

2.F. Balance of Fluid Pressure

To find the balance of fluid pressure, we set the variation of the Lagrangian (2.4) with respect to $\tilde{\phi}_c$ to 0, while imposing the constraint that the volume fractions must sum to 1 (Section 2.C). This provides the relation:

$$\phi_{0c} \frac{\partial W_{0c}}{\partial \phi_c} = \phi_{0b} \frac{\partial W_{0b}}{\partial \phi_b} \tag{2.10}$$

Using the relation that the pressure is related to the Helmholtz free energy density per unit volume by $p = W(\rho) - \rho \dfrac{\mathrm{d}W}{\mathrm{d}\rho}$, we have that $\phi_{0c} \dfrac{\partial W_{0c}}{\partial \phi_c} = J p_{0c}$ and $\phi_{0c} \dfrac{\partial W_{0b}}{\partial \phi_b} = p + p_{0b}$ [50], where p_{0b} is the initial pressure of brine. Combining these relations results in the balance of fluid pressure, i.e., the fluid pressure in the brine is equal to the fluid pressure in the CO$_2$. For the vdW model, we can write this explicitly.

$$-\frac{RT\rho_c}{1 - b\rho_c} + a\rho_c^2 + p + p_{0b} = 0 \tag{2.11}$$

We note that we have ignored capillary pressure effects but including these effects would not change the overall structure of our argument.

2.G. Non-negativity of Dissipation

To ensure compatibility with thermodynamics, it is sufficient in the isothermal setting to ensure that the dissipation is non-negative for any process [48, 51]. Following [43, 52–54], we compute the time derivative of the energy from (2.1):

$$\frac{\mathrm{d}\mathcal{E}}{\mathrm{d}t} = \int_{\Omega_0} \left(\delta_{\boldsymbol{x}} \mathcal{E} \frac{\mathrm{d}\boldsymbol{x}}{\mathrm{d}t} + \delta_{\mathcal{R}_{0c}} \mathcal{E} \frac{\mathrm{d}\mathcal{R}_{0c}}{\mathrm{d}t} + \delta_{\phi_c} \mathcal{E} \frac{\mathrm{d}\phi_c}{\mathrm{d}t} \right) \mathrm{d}\Omega_0 \tag{2.12}$$

where $\delta_{(\cdot)}\mathcal{E}$ is the variational derivative of $\mathcal{E}$ with respect to $(\cdot)$.

In our approach, we have set $\delta_{\boldsymbol{x}}\mathcal{E} \equiv \boldsymbol{0}$ to obtain linear momentum balance, and $\delta_{\phi_c}\mathcal{E} \equiv 0$ t obtain fluid pressure balance. Further, substituting for $\dfrac{\mathrm{d}\mathcal{R}_{0c}}{\mathrm{d}t}$ from (2.7) and using that $\boldsymbol{q}_{0c} = \mathcal{R}_c \boldsymbol{v}_{0c} = -\boldsymbol{K}_c \nabla_0 \delta_{\mathcal{R}_{0c}}\mathcal{E}$, we can write:

$$\frac{\mathrm{d}\mathcal{E}}{\mathrm{d}t} = \int_{\Omega_0} \delta_{\mathcal{R}_{0c}}\mathcal{E}\,\frac{\mathrm{d}\mathcal{R}_{0c}}{\mathrm{d}t}\,\mathrm{d}\Omega_0 = \int_{\Omega_0} \delta_{\mathcal{R}_{0c}}\mathcal{E}\,\mathrm{div}_0\left(\boldsymbol{K}_c \nabla_0 \delta_{\mathcal{R}_{0c}}\mathcal{E}\right)\,\mathrm{d}\Omega_0 = -\int_{\Omega_0} \nabla_0 \delta_{\mathcal{R}_{0c}}\mathcal{E} \cdot \boldsymbol{K}_c \nabla_0 \delta_{\mathcal{R}_{0c}}\mathcal{E}\,\mathrm{d}\Omega_0 \tag{2.13}$$

where we have used integration-by-parts to obtain the final expression. From the positive-definiteness of $\boldsymbol{K}_c$ we have that the integrand is non-negative pointwise above, leading to the conclusion that $\dfrac{\mathrm{d}\mathcal{E}}{\mathrm{d}t} \leq 0$ for every process, in accord with thermodynamics.

2.H. Weak Form and Finite Element Implementation

Our numerical solution is performed using the Finite Element Method in the open-source framework FEniCS [55].

We have six unknowns: $\boldsymbol{x}$, $\mathcal{R}_{0c}$, $\mathcal{R}_{0b}$, $\tilde{\phi}_c$, p, and ψ. We denote the corresponding test functions by $\hat{\boldsymbol{u}}$, $\hat{\mathcal{R}}_c$, $\hat{\mathcal{R}}_b$, $\hat{\Phi}$, $\hat{p}$, and $\hat{\Psi}$. These are governed by 3 PDEs, 2 pointwise constraints, and one substitution to provide a mixed method to deal with higher-order derivatives. The weak forms are as follows:

$$\text{Momentum Balance (2.8):} \quad \int_{\Omega_0} \left(-\boldsymbol{T}\cdot\nabla_0\hat{\boldsymbol{u}} + \boldsymbol{b}_0\cdot\hat{\boldsymbol{u}}\right)\,\mathrm{d}\Omega_0 + \int_{\partial\Omega_0} (\boldsymbol{T}\boldsymbol{n})\cdot\hat{\boldsymbol{u}}\,\mathrm{d}S = \boldsymbol{0} \tag{2.14}$$

$$\text{CO2 Transport (2.7):} \quad \int_{\Omega_0} \left(-\boldsymbol{q}_{0c}\cdot\nabla_0\hat{\mathcal{R}}_c + \frac{\mathcal{R}_{0c}^{n} - \mathcal{R}_{0c}^{n-1}}{\mathrm{d}t}\hat{\mathcal{R}}_c\right)\mathrm{d}\Omega_0 + + \int_{\partial\Omega_0} (\boldsymbol{q}_{0c}\cdot\boldsymbol{n})\,\hat{\mathcal{R}}_c\,\mathrm{d}S = 0 \tag{2.15}$$

$$\text{Brine Transport (2.7):} \quad \int_{\Omega_0} \left(-\boldsymbol{q}_{0b}\cdot\nabla_0\hat{\mathcal{R}}_b + \frac{\mathcal{R}_{0b}^{n} - \mathcal{R}_{0b}^{n-1}}{\mathrm{d}t}\hat{\mathcal{R}}_b\right)\mathrm{d}\Omega_0 + + \int_{\partial\Omega_0} (\boldsymbol{q}_{0b}\cdot\boldsymbol{n})\,\hat{\mathcal{R}}_b\,\mathrm{d}S = 0 \tag{2.16}$$

$$\text{Incompressibility of Brine (2.4):} \quad \int_{\Omega_0} \left(J\phi_{0s} + \tilde{\phi}_c + \frac{\mathcal{R}_{0b}}{\rho_b} - J\right)\hat{\Phi}\,\mathrm{d}\Omega_0 = 0 \tag{2.17}$$

$$\text{Fluid Pressure Balance (2.11):} \quad \int_{\Omega_0} \left(-\frac{RT\rho_c}{1-b\rho_c} + a\rho_c^2 + p + p_{0b}\right)\hat{p}\,\mathrm{d}\Omega_0 = 0 \tag{2.18}$$

$$\text{The substitution } \psi := \mathrm{div}_0\left(\nabla_0\mathcal{R}_{0c}\right)\text{:} \quad \int_{\Omega_0} \left(\psi\hat{\Psi} + \nabla_0\mathcal{R}_{0c}\cdot\nabla_0\hat{\Psi}\right)\mathrm{d}\Omega_0 - \int_{\partial\Omega_0} \hat{\Psi}\nabla_0\mathcal{R}_{0c}\cdot\boldsymbol{n}\,\mathrm{d}S = 0 \tag{2.19}$$

where $\boldsymbol{n}$ is the unit normal to the boundary $\partial\Omega_0$.

We use a triangular mesh with roughly constant refinement throughout the domain. We use continuous interpolations of order 1 for $\boldsymbol{x}$, $\hat{\mathcal{R}}_{0c}$, $\hat{\mathcal{R}}_{0b}$, and $\tilde{\phi}_c$; discontinuous Galerkin (DG) interpolations of order 0, which are piecewise constant within each element, for p; and DG interpolations of order 1, which are piecewise linear, for ψ. This follows the general heuristic that Lagrange multipliers are interpolated at lower-order to satisfy the inf-sup condition [56].

For time evolution, we use an implicit Euler finite-difference scheme and use Newton methods to solve the resulting nonlinear problem at each time step.

3. Numerical Results

3.A. CO_2 Injection into an Underground Layer

We consider a model situation of CO_2 injection from a well into an underground saline layer and find that CO_2 propagation into the layer slows down if phase transformations occur.

We consider a porous layer at the depth of $500\ \mathrm{m}$, which is initially saturated with brine at an initial pressure of $p_0 = 6\,\mathrm{MPa}$. We consider porosity of 0.2 ($\phi_s = 0.8$), and inject super-critical CO_2 from the right boundary with constant rate $q_c = 0.088\ \mathrm{kg/m^2\,s}$. We assume a symmetric domain in the left and right side of the injection well with the geometry and boundary conditions shown in Figure 1, and the material properties of the solid skeleton, brine, and CO_2 are listed in Table 1. We use $\epsilon = 0.01$.

Figure 2 illustrates the variation of CO_2 pressure versus the inverse of CO_2 density ρ_c^{-1} at different temperatures, at various points along the horizontal dashed line shown in Figure 1; as expected, it resembles closely the vdW phase diagram. In this calculation, for simplicity, we do not consider heat transfer between CO_2 and the porous medium following [34], and the temperature consequently refers to the temperature of CO_2. We consider temperatures below and above the CO_2 critical temperature ($T_c = 303.4\,\mathrm{K}$). Our results show that close to the injection well and for temperatures below the critical temperature ($T < T_c$), CO_2 experiences a phase transition from liquid to gas phase. The dashed lines in Figure 2 represent the saturated liquid line, critical point, and saturated gas line. We find that for lower temperatures, CO_2 experiences a sharper change in pressure.

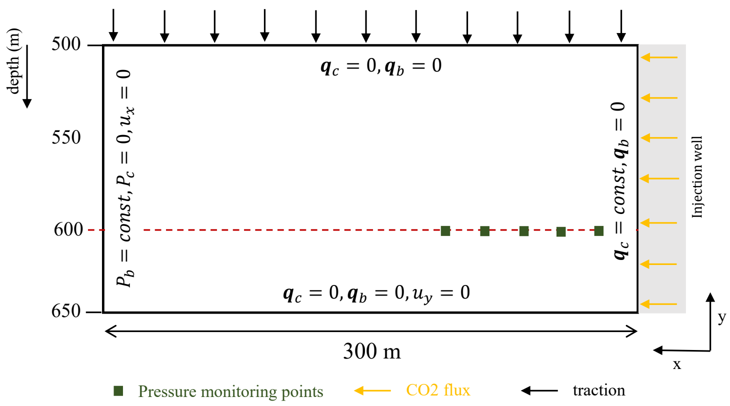

Figure 1. The geometry of the porous layer and injection well.

Property	Value
Solid phase Lame constant, λ	$144.2\,\mathrm{MPa}$
Solid phase Lame constant, μ	$96.1\,\mathrm{MPa}$
Solid density, ρ_s	$2000\,\mathrm{kg/m^3}$
Intrinsic permeability, κ	$2 \times 10^{-12}\,\mathrm{m^2}$
Brine density, ρ_b	$1100\,\mathrm{kg/m^3}$
Brine viscosity, γ_b	$0.001\,\mathrm{Pa\,s}$
CO2 viscosity, γ_c	$3 \times 10^{-5}\,\mathrm{Pa\,s}$
Gas constant, $\bar{R}$	$8.32\,\mathrm{m^3.Pa/K.mol}$
CO_2 constant, a	$0.364\,\mathrm{Pa\,m^6/mol^2}$
CO_2 constant, b	$42.67 \times 10^{-6}\,\mathrm{m^3/mol}$
Critical temperature, T_c	$303.4\,\mathrm{K}$
Gravitational acceleration, g	$10\,\mathrm{m/s^2}$

Table 1. Properties of the solid phase, brine, and CO_2.

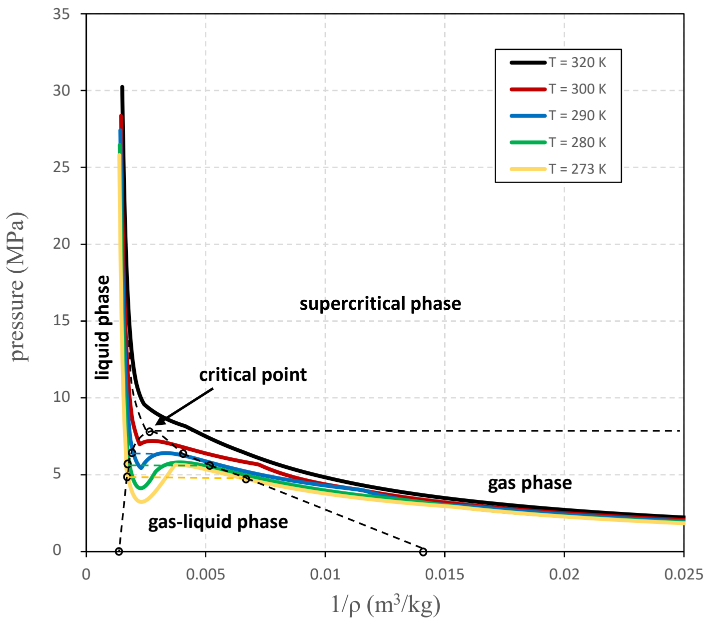

Figure 2. CO_2 pressure v. the inverse of CO_2 density at different temperatures at $t = 10\,000\,\mathrm{s}$. Dashed lines represent the phase boundaries.

Figure 3 shows the CO_2 pressure versus distance from the injection well for different temperatures at a depth of $600\,\mathrm{m}$ (the red dashed line shown in Figure 1) and at $10\,000\,\mathrm{s}$ after injection initiation. Our findings clearly show the phase transition of CO_2 close to the injection point for temperature values below the CO_2 critical temperature. The distance from the well is not sensitive to the injection temperature over the range studied.

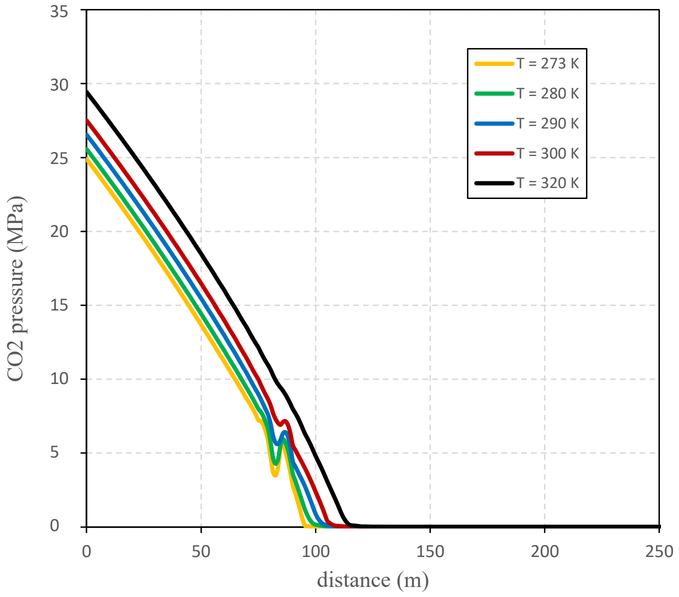

Figure 3. CO_2 pressure (p_c) v. distance at different temperatures at $t = 10\,000\,\mathrm{s}$, and at depth $600\,\mathrm{m}$.

Figure 4 shows the CO_2 density ρ_c versus distance from the injection well for different temperatures at $10\,000\,\mathrm{s}$ after the start of injection. The abrupt change in the CO_2 density highlights clearly the interface between the gas and liquid phases; thus, at $10\,000\,\mathrm{s}$ after injection the interface has migrated to approximately $85\,\mathrm{m}$ away from the injection well. We find that for lower temperatures, CO_2 experiences a larger jump in density. Based on this plot, we can precisely locate the phase transition interface at different temperatures.

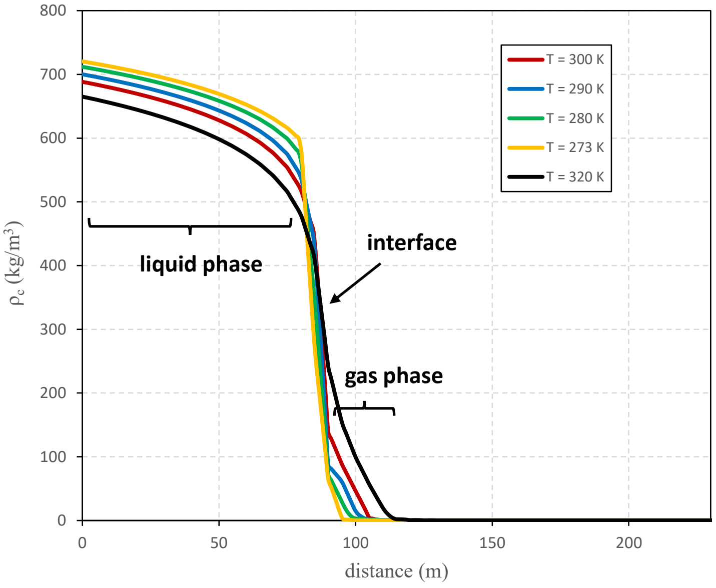

Figure 4. CO_2 density ρ_c v. distance for different temperatures at $t = 10\,000\,\mathrm{s}$, and at depth $600\,\mathrm{m}$.

Figure 5 shows the total fluid pressure versus time at distances from the injection well for the monitoring points shown in Figure 1. The pressure increases with time throughout the domain near the injection well once the plume migrates to a monitoring location. As expected, the points closer to the injection well have higher fluid pressures.

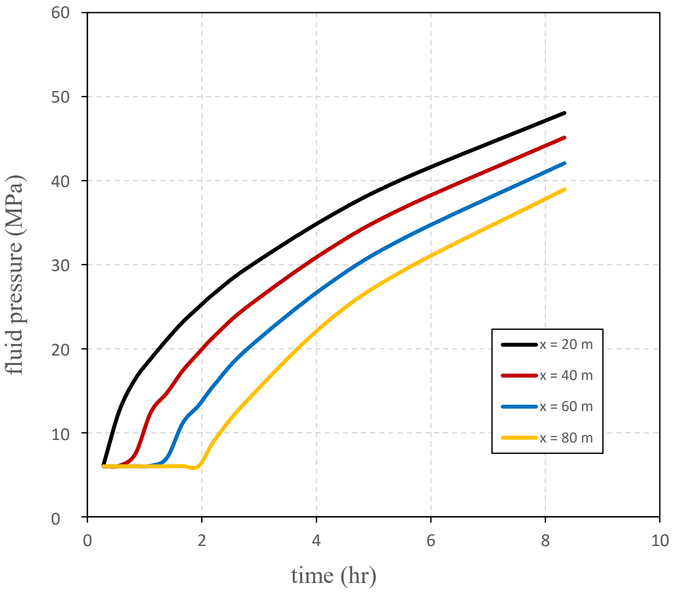

Figure 5. Total fluid pressure v. time at different distances from the injection well at depth 600 m.

Figure 6 shows the CO_2 saturation – defined as $S_c = \phi_c/(1 - \phi_s)$ – contours for two temperatures, one below ($T = 280\,\mathrm{K}$) and one above ($T = 320\,\mathrm{K}$) the critical temperature. This Figure compares the CO2 migration in the reservoir under super-critical ($T = 320\,\mathrm{K}$) and sub-critical conditions ($T = 280\,\mathrm{K}$). In this simulation, CO_2 in injected to a brine saturated reservoir with initial pressure less than the critical pressure of CO_2. In the supercritical case (Fig. 6, left), CO_2 undergoes phase transition from supercritical to gas phase, as the migration in the reservoir. In the sub-critical condition (Fig. 6, right) CO_2 undergoes a phase transition from liquid to gas phase. We find that the phase transformation CO_2 in the subcritical phase causes to slower propagation in the reservoir.

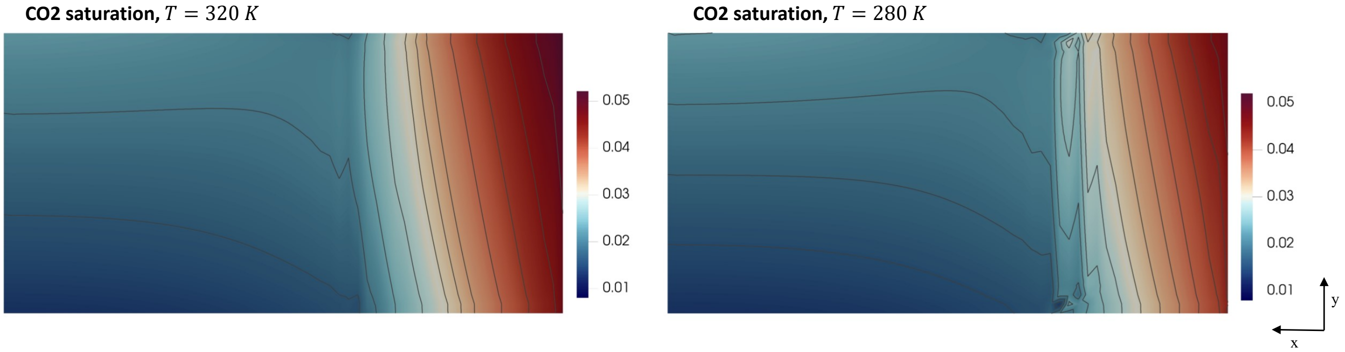

Figure 6. CO_2 saturation contours at $t = 10\,000\,\mathrm{s}$ for temperatures above (320 K, left) and below (280 K, right) the critical temperature.

3.B. Upward Mobility of CO_2 in a Reservoir

In this section, we investigate the upward mobility of CO_2 in a reservoir by injecting CO_2 in the corner of the domain. In a geological reservoir, CO_2 leakage through faults and movement upward to shallower depths decreases the pressure and temperature of the fluid. Therefore, CO_2 experiences sub-critical conditions which can result in forming a mixture of gas-liquid phases. We consider temperatures both above and below the critical temperature of CO_2 to compare the upward mobility of CO_2 in the super and sub-critical conditions. We find that if CO_2 experiences a phase transition, the upward mobility of CO_2 decreases.

For the simulations, the assumed geometry and boundary conditions are shown in Figure 7. We use a constant CO_2 injection rate of $q_c = 0.0088\,\mathrm{kg/m^2s}$ at the right-bottom corner of the reservoir. We consider a $200\,\mathrm{m} \times 100\,\mathrm{m}$ reservoir, which is initially saturated with brine at an initial pressure of $6\,\mathrm{MPa}$. The properties of the solid skeleton, brine, and CO_2 are from Table 1.

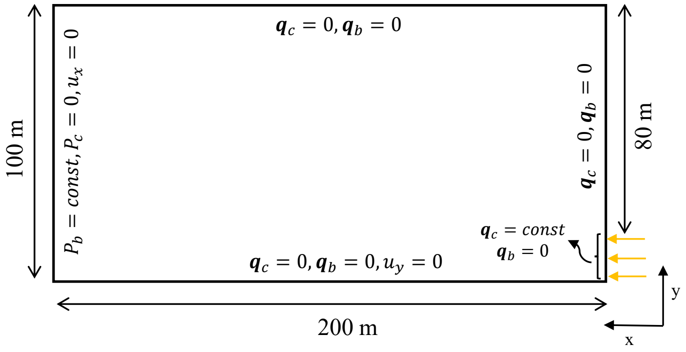

Figure 7. Geometry and boundary condition of the reservoir.

Figure 8 compares the simulations considering T =320 K (without phase transition), and T =290 K (with phase transition) to investigate the effect of CO_2 phase change on the upward mobility and migration of CO_2 in the reservoir. The saturation profiles in Figure 8 show that as the injection continues, CO_2 migrates to the upper parts of the reservoir due to gravity and the difference in the densities of CO_2 and resident fluid (brine). At T =320 K, when the CO_2 is in the super-critical phase, CO_2 propagates faster in the domain. In the sub-critical condition at T =290 K, due to the phase transition of CO_2 that forms a gas-liquid mixture and a significant increase of density, we see a slower migration rate and lower value of saturation.

In these simulations, we assumed that the viscosity of CO_2 is constant. However, in real soils, the viscosity typically varies, with the liquid phase having a higher viscosity, so it would act to further decrease the mobility of gas-liquid CO_2 in comparison to the super-critical phase. However, if CO_2 undergoes a complete transition to the gas phase under sub-critical conditions, the migration mobility of CO_2 will increase in the geological reservoir in comparison to the super-critical phase [41]. We note that, in general, the CO_2 saturation depends on the elastic properties of the solid skeleton, permeability, injection rate, and temperature.

Figure 9 shows the CO_2 density profile considering (T =290 K), below the critical temperature of CO_2. We find a clear signature of the migrating interface between the CO_2 liquid and gas phases during the injection as it propagates both upward and horizontally.

4. Concluding Remarks

In this study, we used a variational energy-based poromechanics model [32] to simulate CO_2 sequestration in a porous deformable medium. An important advantage of the proposed variational formulation is that we can use the van der Waals model for CO_2 to model the phase change in a consistent thermomechanical formulation. It consequently enables us to conduct an investigation of the complex behavior of the CO_2 gas-liquid mixture, the moving interface between gas and liquid phases, and the sharp change in the CO_2 saturation profile due to the phase change, during the injection and migration into geological formations. We use the model to compute the pressure, density, and CO_2 saturation distributions after injecting dense CO_2 into an underground saline formation and examine the liquid-gas CO_2 phase transition and its effect on pressure and saturation profiles at different temperatures.

We studied numerically two model problems that correspond to simplified versions of realistic injection processes. First, we modeled CO_2 injection from a well into an underground saline layer and found that CO_2 propagation into the layer slows down if phase transformations occur. Second, we investigated the upward mobility of CO_2 in a reservoir and found that if CO_2 experiences a phase transition to form a mixture of gas and liquid phases, the upward mobility of CO_2 decreases. Finally, we note certain limitations of our work and outline potential future directions. First, heat exchange between the fluid phases and the solid porous domain is a significant effect, and the model can be extended beyond the isothermal setting. Second, while our current assumptions include a constant viscosity for CO_2, the model can be extended by considering viscosity changes associated with phase transformations. Finally, although our focus has been on a two-phase flow, the energetic formulation allows us to study unsaturated systems by introducing an additional gas phase.

Acknowledgments. We thank NSF for XSEDE resources provided by Pittsburgh Supercomputing Center, and John Clayton and Ruby Fu for helpful discussions. Mina Karimi acknowledges financial support from the Scott Institute for Energy Innovation and the Dowd Fellowship from the College of Engineering at Carnegie Mellon University. Kaushik Dayal acknowledges financial support from NSF (DMS 2108784) and ARO (MURI W911NF-24-2-0184), and an appointment to the National Energy Technology Laboratory sponsored by the U.S. Department of Energy. Matteo Pozzi acknowledges financial support from NSF (CMMI 1638327). Noel Walkington acknowledges financial support from NSF (DMS 1729478 and DMS 2012259).

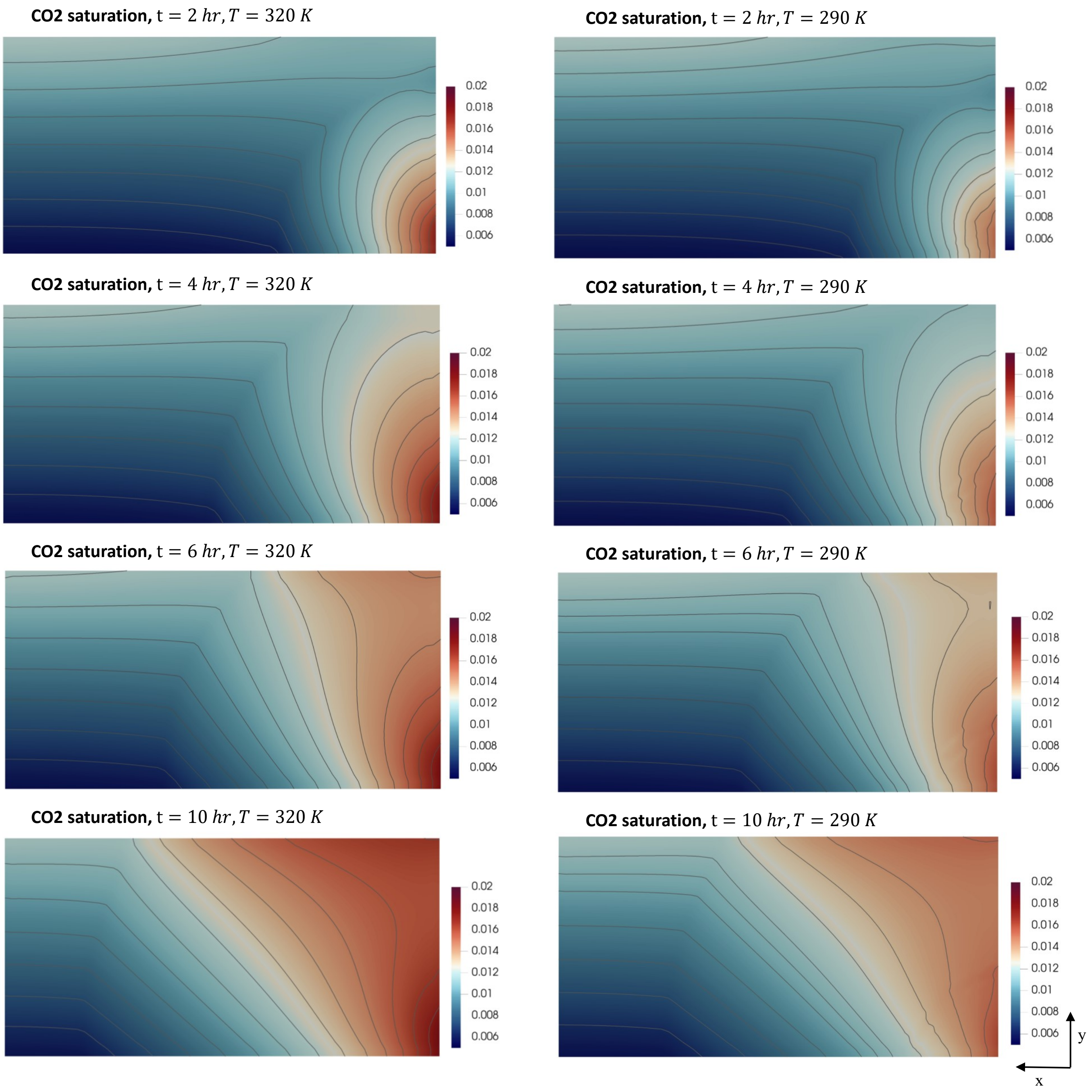

Figure 8. CO_2 saturation profiles during injection at super-critical $T = 320\,\mathrm{K}$ (left) and sub-critical $T = 290\,\mathrm{K}$ (right) conditions.

Data Sharing. A version of the code developed for this work is available at `doi.org/10.5281/zenodo.10820190`

Competing Interest Statement. The authors declare no competing interest.

A. The Peng-Robinson Model for CO_2

In this section, we demonstrate the ability of the approach to handle different free energy functions. Specifically, we use the Peng-Robinson free energy [57] to simulate CO_2. The Peng-Robinson has a better fit than vdW to the properties of CO_2, at the

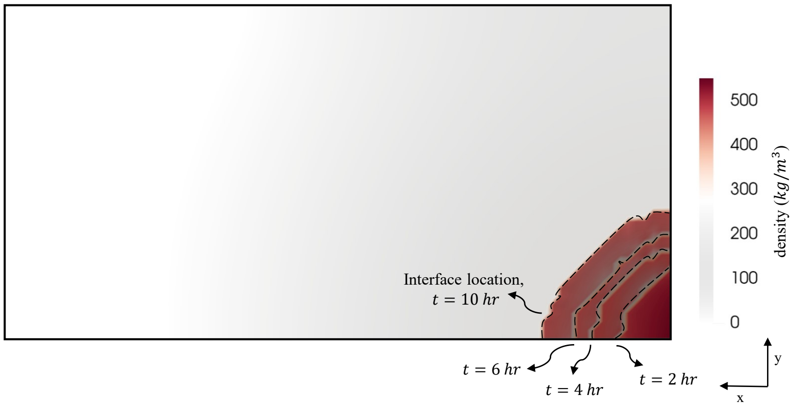

Figure 9. CO_2 density profiles and the migrating interface between the CO_2 liquid and gas phases during the first 10 hours of injection, at $T = 290\,\mathrm{K}$.

cost of introducing more empirical features.

$$W_{0c}(\mathcal{R}_{0c}, \phi_c, J) = c\mathcal{R}_{0c}\bar{R}T\left(1 - \log(c\bar{R}T)\right) - \mathcal{R}_{0c}\bar{R}T\log\left(\frac{J\phi_c}{\mathcal{R}_{0c}} - b\right) - \frac{a\alpha\mathcal{R}_{0c}}{2b\sqrt{2}}\log\left(\frac{\sqrt{2} + \left(\frac{b\mathcal{R}_{0c}}{J\phi_c} - 1\right)}{\sqrt{2} - \left(\frac{b\mathcal{R}_{0c}}{J\phi_c} - 1\right)}\right) \tag{A1}$$

where $\bar{R}$ is the ideal gas constant, c is a non-dimensional constant, a, b and α are constants that relate to the phase transition and are defined as follows:

$$a = 0.4572\frac{\bar{R}^2T_c^2}{P_c}, \quad b = 0.0778\frac{\bar{R}T_c}{P_c}, \quad \alpha = \left(1 + m\left(1 - \sqrt{\frac{T}{T_c}}\right)\right), \text{ where } m = 0.3746 + 1.5422w - 0.2699w^2$$

where T_c and P_c are critical temperature and pressure of CO_2, respectively, and w is the acentric factor of of the fluid.

We substitute the Peng-Robinson free energy (A1) in the Lagrangian functional (2.4), and obtain the chemical potential of CO_2 by taking the variational derivative of Lagrangian with respect to $\mathcal{R}_{0c}$:

$$\eta_{0c} = -c\bar{R}T\left(1 - \log(c\bar{R}T)\right) + \bar{R}T\log\left(\frac{1}{\rho_c} - b\right) - \frac{\bar{R}T}{1 - b\rho_c} + \frac{a\alpha}{2b\sqrt{2}}\log\left(\frac{\sqrt{2} + (b\rho_c - 1)}{\sqrt{2} - (b\rho_c - 1)}\right) \tag{A2}$$

We further obtain the balance of fluid pressure by setting to zero the variational derivative of the Lagrangian with respect to $\tilde{\phi}_c$:

$$-\frac{RT\rho_c}{1 - b\rho_c} + \frac{a\alpha\rho_c^2}{1 - b^2\rho_c^2 + 2b\rho_c} + p + p_{0b} = 0 \tag{A3}$$

Figure 10 compares the saturation profiles resulting from vdW and Peng-Robinson models. In this simulation, the temperature is set to $= 320\ K$, and the material properties and the vdW constants are taken from table 1. For the Peng-Robinson model, we assume $w = 0.224$. The boundary and initial conditions are assumed to be similar to section 3.B.

B. Comparison with Conventional Multiphase Models

The movement of CO_2 and brine, assumed as two immiscible fluid phases, has been studied using the conventional multiphase method. This method combines an extended form of Darcy's law with mass conservation equations [58, 59]. The multiphase extension of Darcy's law describes the relative velocity of each immiscible phase as follows [60, 61]:

$$\boldsymbol{v}_i = -\frac{kk_{ri}}{\mu_i}\left(\nabla p_i - \rho_i\boldsymbol{g}\right) \tag{B1}$$

where k is the true permeability of the medium, and k_{ri} is the relative permeability of each phase. The relative permeability is a function of saturation S_i and varies between zero and one, i.e., $0 < k_{ri}(S_i) < 1$. The function $k_{ri}(S_i)$ is typically determined empirically based on experimental measurements. For details on different relative permeability relations, we refer to [60].

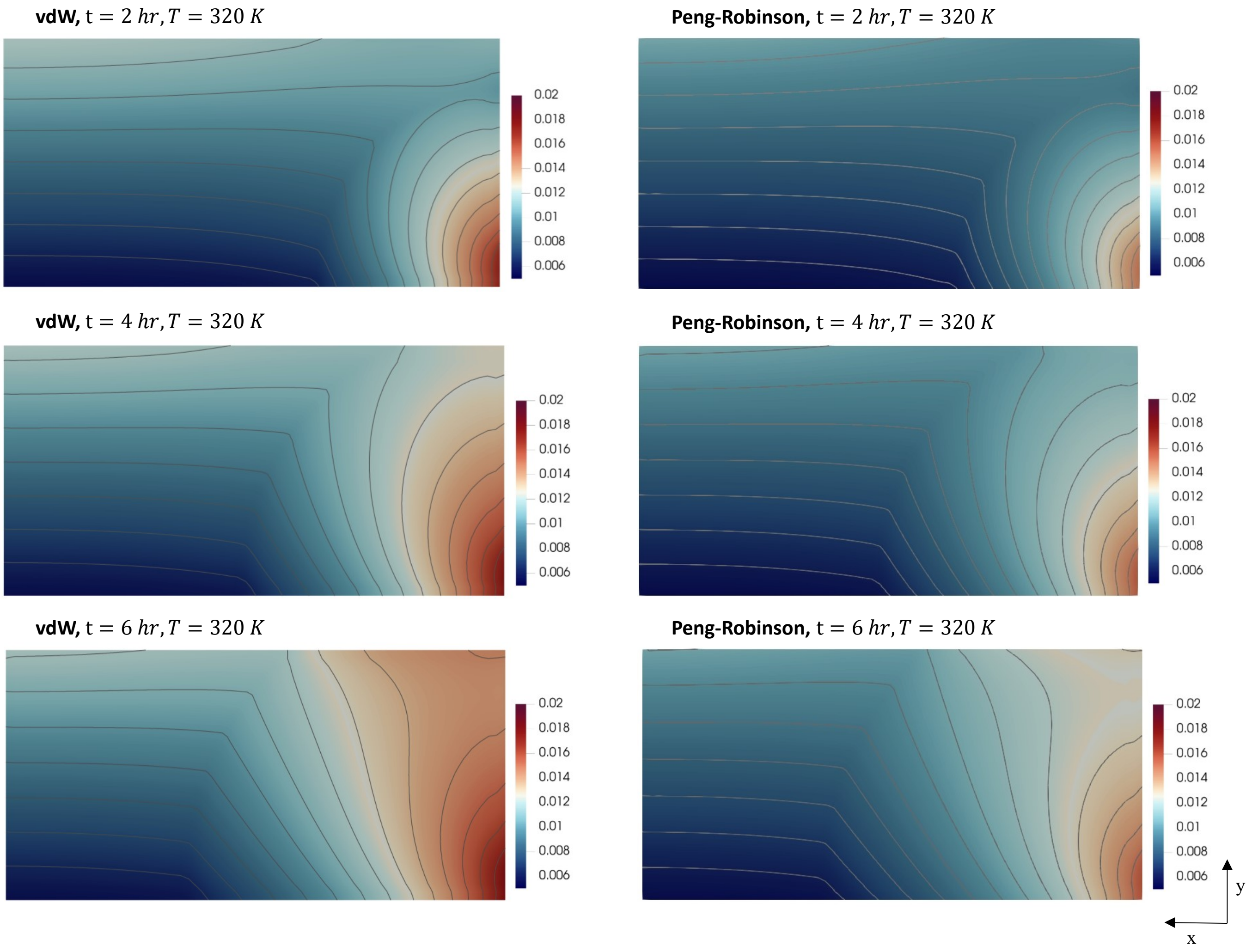

vdW, t = 2 hr, T = 320 K

Peng-Robinson, t = 2 hr, T = 320 K

vdW, t = 4 hr, T = 320 K

Peng-Robinson, t = 4 hr, T = 320 K

vdW, t = 6 hr, T = 320 K

Peng-Robinson, t = 6 hr, T = 320 K

Figure 10. Comparison of CO$_2$ saturation profiles using the vdW model (right) and the Peng-Robinson model (left), at a temperature $T = 320\ K$.

The conservation of mass for each fluid phase can be written as

$$\frac{\partial}{\partial t}\left(\phi_i \rho_i\right) + \mathrm{div}(\rho_i \boldsymbol{v}_i) = 0 \tag{B2}$$

where ϕ_i is the porosity of each fluid phase and can be defined as $\phi_i = \phi S_i$, where ϕ is the porosity of medium and for simplicity can be assumed constant. Under this assumption, the system has six unknowns: S_c, S_b, ρ_c, ρ_b, p_c, and p_b, where subscripts c, and b refer to CO$_2$ and brine phases. The system is constrained by the saturation condition $S_c + S_b = 1$. The compressibility conditions for each fluid phase relate the density of each fluid phase to pressure. Additionally, the capillary pressure, $p_{\text{capillary}} = p_c - p_b$, provides a relationship between the CO$_2$ and brine pressure. $p_{\text{capillary}}(S_i)$ is a function of saturation, which follows empirical relations such as Brooks–Corey [33].

In this work, we neglect the capillary pressure. Based on the van der Waals (vdW) free energy, the pressure of CO$_2$ is a function of ρ_c. We note that our definition of the flux and velocity vectors for each fluid phase (Section 2.D) leads to a linear relative permeability formulation, given by $k_{ri} = \phi S_i$. However, the framework in this paper is general and can be adapted to incorporate capillary pressure effects, nonlinear relative permeability relations, and compressibility of the brine phase, which are topics for future work.

[1] National Academies of Sciences Engineering and Medicine. *Negative Emissions Technologies and Reliable Sequestration: A Research Agenda*. The National Academies Press, Washington, DC, 2019.

[2] Wei-Yin Chen, Toshio Suzuki, and Maximilian Lackner. *Handbook of climate koli mitigation and adaptation*. Springer International Publishing, 2017.

[3] CM Oldenburg, Karsten Pruess, and Sally M Benson. Process modeling of CO2 injection into natural gas reservoirs for carbon sequestration and enhanced gas recovery. *Energy & Fuels*, 15(2):293–298, 2001.

[4] Nawaz Ahmad, Anders Wörman, Xavier Sanchez-Vila, Jerker Jarsjö, Andrea Bottacin-Busolin, and Helge Hellevang. Injection of CO2-saturated brine in geological reservoir: A way to enhanced storage safety. *International journal of greenhouse gas control*, 54:129–144, 2016.

[5] X Fu, L Cueto-Felgueroso, D Bolster, and R Juanes. Rock dissolution patterns and geochemical shutdown of–brine–carbonate reactions during convective mixing in porous media. *Journal of Fluid Mechanics*, 764:296–315, 2015.

[6] Anastasia G Ilgen, Pania Newell, Tomasz Hueckel, D Nicolas Espinoza, and Manman Hu. Coupled chemical-mechanical processes associated with the injection of CO2 into subsurface. In *Science of carbon storage in deep saline formations*, pages 337–359. Elsevier, 2019.

[7] Victor N Balashov, George D Guthrie, Christina L Lopano, J Alexandra Hakala, and Susan L Brantley. Reaction and diffusion at the reservoir/shale interface during CO2 storage: Impact of geochemical kinetics. *Applied Geochemistry*, 61:119–131, 2015.

[8] Nawaz Ahmad. *REACTIVE TRANSPORT MODELLING OF DISSOLVED CO2 IN POROUS MEDIA: Injection into and leakage from geological reservoirs*. PhD thesis, KTH Royal Institute of Technology, 2016.

[9] Jiaan Wang, Wei Xiong, James B Gardiner, Brandon C McAdams, Brian W Stewart, R Burt Thomas, J Alexandra Hakala, Christina L Lopano, and Mitchell J Small. A geochemically informed leak detection (gild) model for CO2 injection sites. *Applied Geochemistry*, page 105691, 2023.

[10] Mina Karimi and Kaushik Bhattacharya. A learning-based multiscale model for reactive flow in porous media. *Water Resources Research*, 60(9):e2023WR036303, 2024.

[11] Víctor Vilarrasa, Jesus Carrera, Sebastià Olivella, Jonny Rutqvist, and Lyesse Laloui. Induced seismicity in geologic carbon storage. *Solid Earth*, 10(3):871–892, 2019.

[12] Jonny Rutqvist, Antonio P Rinaldi, Frederic Cappa, Pierre Jeanne, Alberto Mazzoldi, Luca Urpi, Yves Guglielmi, and Victor Vilarrasa. Fault activation and induced seismicity in geological carbon storage–lessons learned from recent modeling studies. *Journal of Rock Mechanics and Geotechnical Engineering*, 8(6):789–804, 2016.

[13] Kyung Won Chang, Hongkyu Yoon, Mario J Martinez, and Pania Newell. Coupled hydro-mechanical modeling of injection-induced seismicity in the multiphase flow system. In *53rd US Rock Mechanics/Geomechanics Symposium*. OnePetro, 2019.

[14] Pania Newell and Mario J Martinez. Numerical assessment of fault impact on caprock seals during CO2 sequestration. *International Journal of Greenhouse Gas Control*, 94:102890, 2020.

[15] Seyyed Abolfazl Hosseini, Simon A Mathias, and Farzam Javadpour. Analytical model for CO2 injection into brine aquifers-containing residual CH4. *Transport in porous media*, 94(3):795–815, 2012.

[16] Zhao-Qin Huang, Philip H Winterfeld, Yi Xiong, Yu-Shu Wu, and Jun Yao. Parallel simulation of fully-coupled thermal-hydro-mechanical processes in CO2 leakage through fluid-driven fracture zones. *International Journal of Greenhouse Gas Control*, 34:39–51, 2015.

[17] Thomas Giorgis, Michele Carpita, and Alfredo Battistelli. 2d modeling of salt precipitation during the injection of dry CO2 in a depleted gas reservoir. *Energy Conversion and Management*, 48(6):1816–1826, 2007.

[18] Matthias Preisig and Jean H Prévost. Coupled multi-phase thermo-poromechanical effects. case study: CO2 injection at in salah, algeria. *International Journal of Greenhouse Gas Control*, 5(4):1055–1064, 2011.

[19] Fengrui Sun, Yuedong Yao, Xiangfang Li, Guozhen Li, Yanan Miao, Song Han, and Zhili Chen. Flow simulation of the mixture system of supercritical CO2 & superheated steam in toe-point injection horizontal wellbores. *Journal of Petroleum Science and Engineering*, 163:199–210, 2018.

[20] Ardiansyah Negara, MOHAMED FATHY El-Amin, and SHUYU Sun. Simulation of CO2 plume in porous media: consideration of capillarity and buoyancy effects. *International Journal of Numerical Analysis and Modeling, Series B*, 2(4):315–337, 2011.

[21] Avinoam Rabinovich, Kasama Itthisawatpan, and Louis J Durlofsky. Upscaling of CO2 injection into brine with capillary heterogeneity effects. *Journal of Petroleum Science and Engineering*, 134:60–75, 2015.

[22] Hongqing Song, Gang Huang, Tianxin Li, Yu Zhang, and Yu Lou. Analytical model of CO2 storage efficiency in saline aquifer with vertical heterogeneity. *Journal of Natural Gas Science and Engineering*, 18:77–89, 2014.

[23] Jan M Nordbotten and Michael A Celia. Analysis of plume extent using analytical solutions for CO2 storage. `https://dataspace.princeton.edu/handle/88435/dsp01z603qx41q`, 2010.

[24] Roland T Okwen, Mark T Stewart, and Jeffrey A Cunningham. Temporal variations in near-wellbore pressures during CO2 injection in saline aquifers. *International Journal of Greenhouse Gas Control*, 5(5):1140–1148, 2011.

[25] Víctor Vilarrasa, Jesús Carrera, and Sebastià Olivella. Two-phase flow effects on the CO2 injection pressure evolution and implications for the caprock geomechanical stability. *E3S Web Conf.*, 9:04007, 2016.

[26] Jize Piao, Weon Shik Han, Sungwook Choung, and Kue-Young Kim. Dynamic behavior of CO2 in a wellbore and storage formation: wellbore-coupled and salt-precipitation processes during geologic CO2 sequestration. *Geofluids*, 2018, 2018.

[27] Kiseok Kim, Victor Vilarrasa, and Roman Y Makhnenko. CO2 injection effect on geomechanical and flow properties of calcite-rich reservoirs. *Fluids*, 3(3):66, 2018.

[28] Taehyun Kim, Chan-Hee Park, Norihiro Watanabe, Eui-Seob Park, Jung-Wook Park, Yong-Bok Jung, and Olaf Kolditz. Numerical modeling of two-phase flow in deformable porous media: application to CO2 injection analysis in the otway basin, australia. *Environmental Earth Sciences*, 80(3):1–15, 2021.

[29] A-K Singh, N Böttcher, W Wang, C-H Park, U-J Görke, and O Kolditz. Non-isothermal effects on two-phase flow in porous medium: CO2 disposal into a saline aquifer. *Energy Procedia*, 4:3889–3895, 2011.

[30] Gerard A Ateshian and Jay J Shim. Continuum thermodynamics of the phase transformation of thermoelastic fluids. *arXiv preprint arXiv:2207.14158*, 2022.

[31] Tianyi Hu, Hao Wang, and Hector Gomez. Direct van der waals simulation (dvs) of phase-transforming fluids. *arXiv preprint*

arXiv:2212.01983, 2022.

[32] Mina Karimi, Mehrdad Massoudi, Noel Walkington, Matteo Pozzi, and Kaushik Dayal. Energetic formulation of large-deformation poroelasticity. *International Journal for Numerical and Analytical Methods in Geomechanics*, 2022.

[33] Olaf Kolditz, Sebastian Bauer, Norbert Böttcher, Derek Elsworth, U-J Görke, C-I McDermott, C-H Park, Ashok K Singh, J Taron, and Wenqing Wang. Numerical simulation of two-phase flow in deformable porous media: Application to carbon dioxide storage in the subsurface. *Mathematics and Computers in Simulation*, 82(10):1919–1935, 2012.

[34] U-J Goerke, C-H Park, W Wang, AK Singh, and O Kolditz. Numerical simulation of multiphase hydromechanical processes induced by CO2 injection into deep saline aquifers. *Oil & Gas Science and Technology–Revue d'IFP Energies nouvelles*, 66(1):105–118, 2011.

[35] Karsten Pruess. Numerical simulation of CO2 leakage from a geologic disposal reservoir, including transitions from super-to subcritical conditions, and boiling of liquid CO2. *Spe Journal*, 9(02):237–248, 2004.

[36] Karsten Pruess. Integrated modeling of CO2 storage and leakage scenarios including transitions between super-and subcritical conditions, and phase change between liquid and gaseous CO2. *Greenhouse Gases: Science and Technology*, 1(3):237–247, 2011.

[37] Karsten Pruess. ECO2m: a tough2 fluid property module for mixtures of water, NaCl, and CO2, including super-and sub-critical conditions, and phase change between liquid and gaseous CO2. Technical report, Lawrence Berkeley National Lab.(LBNL), Berkeley, CA (United States), 2011.

[38] Meng Lu and Luke Daulton Connell. Transient, thermal wellbore flow of multispecies carbon dioxide mixtures with phase transition during geological storage. *International Journal of Multiphase Flow*, 63:82–92, 2014.

[39] Nian-Hui Wan, Li-Song Wang, Lin-Tong Hou, Qi-Lin Wu, and Jing-Yu Xu. Modeling transient flow in CO2 injection wells by considering the phase change. *Processes*, 9(12):2164, 2021.

[40] Kyuro Sasaki and Yuichi Sugai. *Heat transfer and phase change in deep CO2 injector for CO2 geological storage*. INTECH Open Access Publisher, 2011.

[41] LGH Bert van der Meer, Cor Hofstee, and Bogdan Orlic. The fluid flow consequences of CO2 migration from 1000 to 600 metres upon passing the critical conditions of CO2. *Energy Procedia*, 1(1):3213–3220, 2009.

[42] Victor Vilarrasa and Jonny Rutqvist. Thermal effects on geologic carbon storage. *Earth-science reviews*, 165:245–256, 2017.

[43] S Kiana Naghibzadeh, Anthony Rollett, Noel Walkington, and Kaushik Dayal. Accretion and ablation in deformable solids using an eulerian formulation: A finite deformation numerical method. *Journal of the Mechanics and Physics of Solids*, 200:106076, 2025.

[44] Alessandro Gajo. A general approach to isothermal hyperelastic modelling of saturated porous media at finite strains with compressible solid constituents. *Proceedings of the Royal Society A: Mathematical, Physical and Engineering Sciences*, 466(2122):3061–3087, 2010.

[45] Chao Li, Ronaldo I Borja, and Richard A Regueiro. Dynamics of porous media at finite strain. *Computer methods in applied mechanics and engineering*, 193(36-38):3837–3870, 2004.

[46] Wei Hong, Xuanhe Zhao, Jinxiong Zhou, and Zhigang Suo. A theory of coupled diffusion and large deformation in polymeric gels. *Journal of the Mechanics and Physics of Solids*, 56(5):1779–1793, 2008.

[47] Xiaojing Fu, Luis Cueto-Felgueroso, and Ruben Juanes. Thermodynamic coarsening arrested by viscous fingering in partially miscible binary mixtures. *Physical Review E*, 94(3):033111, 2016.

[48] Rohan Abeyaratne and James K Knowles. *Evolution of phase transitions: a continuum theory*. Cambridge University Press, 2006.

[49] Olivier Coussy. *Poromechanics*. John Wiley & Sons, 2004.

[50] Janel Chua, Mina Karimi, Patrick Kozlowski, Mehrdad Massoudi, Santosh Narasimhachary, Kai Kadau, George Gazonas, and Kaushik Dayal. Deformation Decomposition versus Energy Decomposition for Chemo-and Poro-Mechanics. *Journal of Applied Mechanics*, 91(1):014501, 2024. Publisher: American Society of Mechanical Engineers.

[51] Oliver Penrose and Paul C Fife. Thermodynamically consistent models of phase-field type for the kinetic of phase transitions. *Physica D: Nonlinear Phenomena*, 43(1):44–62, 1990.

[52] Robert Buarque de Macedo, Hossein Pourmatin, Timothy Breitzman, and Kaushik Dayal. Disclinations without gradients: A nonlocal model for topological defects in liquid crystals. *Extreme Mechanics Letters*, 23:29–40, 2018.

[53] Vaibhav Agrawal and Kaushik Dayal. A dynamic phase-field model for structural transformations and twinning: Regularized interfaces with transparent prescription of complex kinetics and nucleation. part i: Formulation and one-dimensional characterization. *Journal of the Mechanics and Physics of Solids*, 85:270–290, 2015.

[54] Vaibhav Agrawal and Kaushik Dayal. A dynamic phase-field model for structural transformations and twinning: Regularized interfaces with transparent prescription of complex kinetics and nucleation. part ii: Two-dimensional characterization and boundary kinetics. *Journal of the Mechanics and Physics of Solids*, 85:291–307, 2015.

[55] FEniCS — fenicsproject.org. `https://fenicsproject.org/`. [Accessed 18-04-2025].

[56] Gilbert Strang. *Computational Science and Engineering*. Wellesley-Cambridge Press, Philadelphia, PA, 2007.

[57] Bruce E Poling, John M Prausnitz, John P O'connell, et al. The properties of gases and liquids, 2001.

[58] Jacob Bear. *Dynamics of fluids in porous media*. Courier Corporation, 2013.

[59] Jan M Nordbotten and Michael A Celia. Similarity solutions for fluid injection into confined aquifers. *Journal of Fluid Mechanics*, 561:307–327, 2006.

[60] Benjamin Court, Karl W Bandilla, Michael A Celia, Adam Janzen, Mark Dobossy, and Jan M Nordbotten. Applicability of vertical-equilibrium and sharp-interface assumptions in co2 sequestration modeling. *International Journal of Greenhouse Gas Control*, 10:134–147, 2012.

[61] Marco Dentz and Daniel M Tartakovsky. Abrupt-interface solution for carbon dioxide injection into porous media. *Transport in Porous Media*, 79:15–27, 2009.